communications materials

A Nature Portfolio journal

Article

https://doi.org/10.1038/s43246-026-01125-w

Multifunctional metallic nanomushrooms on nanowires for detecting and killing tumor cells

Yujie Qi[1,3], Haojian Qiu[1,3], Hailang Dai[1,3] ✉ & Xianfeng Chen [1,2] ✉

The fabrication and advancement of multifunctional nanomaterials have long been a focus of attention in applied research. This is primarily attributed to their ability to integrate multiple desirable properties into a single material system, which not only enhances operational efficiency but also reduces the reliance on complex multi-component systems. Using a facile physical approach, we synthesized multifunctional metallic alloy nanomushrooms on nanowire featuring high-targeting precision and intense photoluminescence. The alloy core of the nanomushrooms, with superior electrical conductivity, significantly improves photothermal conversion efficiency. Meanwhile, their unique mushroom-like morphology enables dense loading of targeting molecules. This design allows simultaneous tumor cell visualization via enhanced fluorescence and their elimination via photothermal ablation. Experimental validation confirms its potential as a theranostic agent, overcoming limitations of current photoluminescent nanomaterials in biomedicine.

In the field of nanotechnology research, there are many nanomaterials and metal nanostructures have gained significant attention due to unique properties. Therein, advanced abilities to engineer their surface chemistry[1–3], methods to create sophisticated multi-dimensional shapes[4–6], own to provide biocompatibility as well as their highly useful optical characteristics[7–10]. Meanwhile, strong localized surface plasmon resonance (LSPR) excited in metal nanostructure, high wideband spectrum absorption coefficients, abundant ligands and surfactants in spatial structure, which increasingly make them applicable in various fields of biomedicine. Thus, hundreds of different types of complex metal nanostructures (e.g., nanostars, nanocages, and branched nanowires) have been explored and utilized as contrast agents for energy utilization and development, high sensitivity of sensing, and nanomedicine, with different sizes, shapes, and compositions. Recently, complex metal nanostructures, which consists of specific numbers of metal atoms and organic ligands, bridge the gap between single metal atom/complex and conventional nanostructures due to the ultrasmall size of less than 3 nm[11–13]. This is based on the principle of the discrete energy level rather than the continuous energy band in the ultrasmall size of nanoparticle, and leads to molecular-like physicochemical properties due to quantum size effect, for example, optical absorption/emission[14–16]. Therein, photoluminescence (PL) of complex metal nanostructure has gained increasing attention in the field of bioimaging[17,18], sensing[19] and optoelectronic devices[20,21]. Notably, PL of complex metal nanostructures requires intricate designs and compositions enabled by sophisticated chemical synthesis techniques. The central fluorescent wavelength of complex metal nanostructures is determined by the proportion of different metal atoms. However, most complex metal nanostructures exhibit much weaker emissions and lower quantum yield (QYs) compared to other types of luminescent materials, such as carbon quantum dots and organic dyes, which substantially hinders the advancement of luminescent complex metal nanostructures towards practical applications. Moreover, these alloy nanostructures have relatively uniform shapes and sizes, which is not conducive to necessary modifications on the surface of the structures, for example, targeted loading and drug loading applied in the biomedical field.

Here, we present a method that growing targeted photoluminescent metallic alloy nanomushrooms on nanowire with simple physical technology. Under electron beam irradiation, mushroom-shaped Au–Ag nanoalloy structures gradually grow on the defect sites of Au–Ag nanowires owing to the activation of Ag atoms migrate, accumulate and undergo compressive stacking. The size of Au–Ag alloy nanomushrooms can be synchronously controlled by adjusting the electron beam irradiation time. These nanostructures possess intrinsic photoluminescent properties, while the molecular-like physicochemical features and LSPR derived from their alloy nature jointly confer favorable plasmonic and

---

[1] School of Physics and Astronomy, Shanghai Jiao Tong University, Shanghai, China. [2] Collaborative Innovation Center of Light Manipulations and Applications, Shandong Normal University, Jinan, China. [3] These authors contributed equally: Yujie Qi, Haojian Qiu, Hailang Dai. ✉e-mail: hailangdai@sjtu.edu.cn; xfchen@sjtu.edu.cn

electronic characteristics on the system. Moreover, the large umbrella-shaped cap of the nanometallic mushrooms offer significantly increased specific surface area compared with bare Au–Ag nanostructures to high-capacity binding sites for ligands, facilitating their robust and receptor-mediated accumulation in target tissues, such as tumor cells. In addition, the dense growth of PL nanomushrooms on the nanowires significantly expands the fluorescent area and enhances emission intensity, thereby improving fluorescence tracking efficiency. Experimental measurements reveal that the metallic nanomushrooms exhibit significantly superior electrical conductivity and photothermal conversion efficiency compared to Au–Ag nanowires due to the enhancement of LSPR. Consequently, the targeted photoluminescent metallic nanomushrooms on the nanowire can simultaneously achieve precise tracking and efficient killing of tumor cells.

Results and discussion

Real-time manipulation of growing metallic nanomushrooms on nanowire

The preparation of Au–Ag nanowire is based on a chemical method (Supporting Information). The metallic nanomushrooms are composed of Au atoms and Ag atoms, as illustrated in Fig. 1. In the TEM images (Fig. 1c–h), the metallic nanomushrooms gradually growing older as the duration of electron beam irradiation increases (Fig. 1c), therein the acceleration voltage of the electron beam is 200 kV, and the current density is generally between 0.6 and 1 nA and the radiation dose is approximately 1200 e/A^{2}s. The metallic nanomushroom grow from a spore-like state into an umbrella-shaped structure, with their volume increasing nearly tenfold (Fig. 1c, d). Meanwhile, the root portion of the metallic nanowires on which the nanomushrooms grow becomes increasingly transparent (Fig. 1d). It is reveal that the metallic nanomushrooms grow by absorbing metal atoms from the nanowire (Fig. 1e, f). According to the element mapping of metallic nanomushroom (Fig. 1g, h), gold atom (yellow) distribution remains unchanged on the nanowire, while silver atoms (red) migrate almost entirely from the nanowires to fuel nanomushroom growth. This results demonstration that electron beam irradiation induces the activation of Ag atoms migrate, accumulate and undergo compressive stacking at the defect sites of Au–Ag nanowires, thereby forming nanoalloy structures, triggering Au nanoparticle expansion via atomic incorporation, facilitated by Au high ductility.

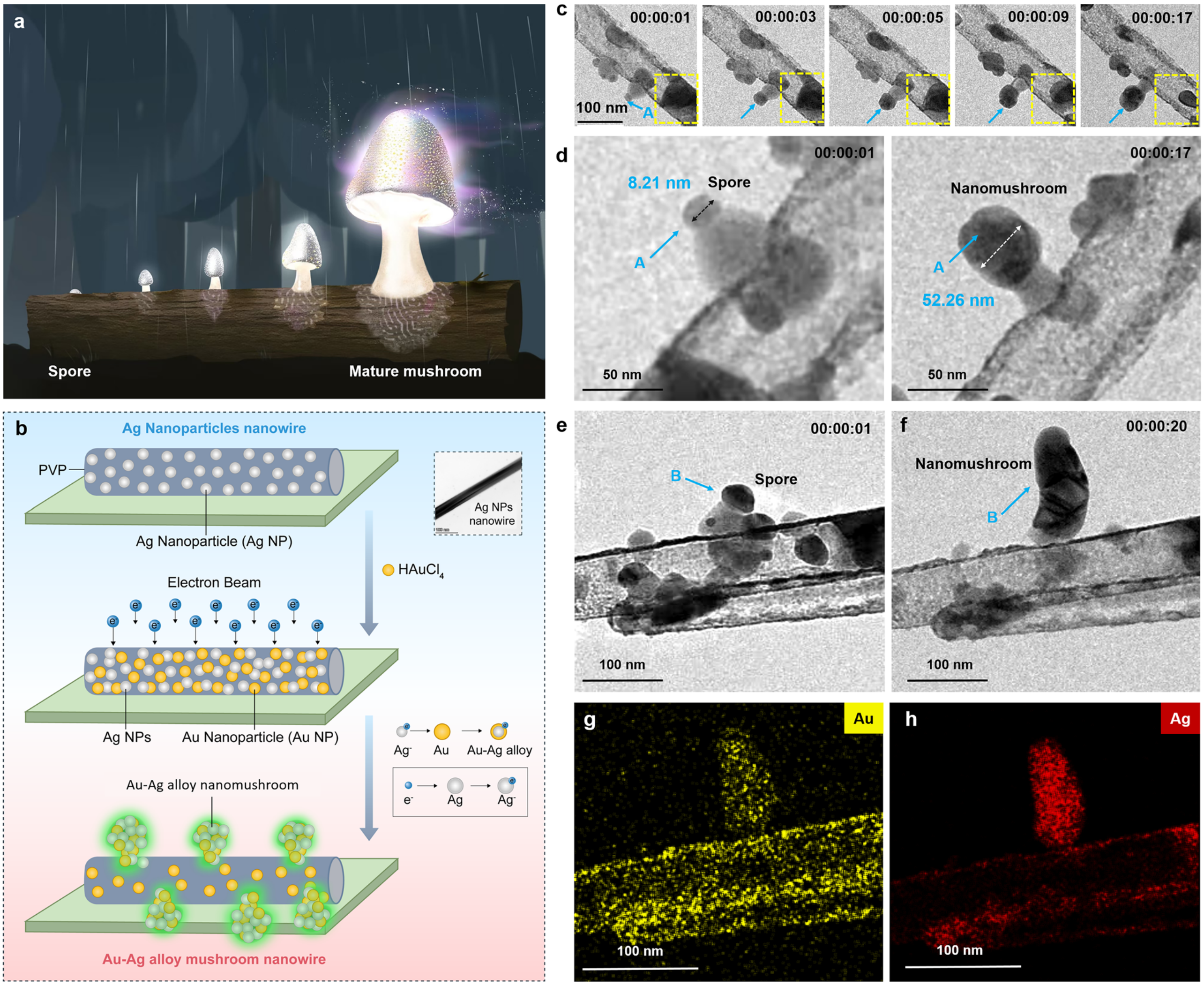

Fig. 1 | Real-time manipulation of growing metallic nanomushrooms on nanowire. a Schematic illustration of growing metallic nanomushrooms on a nanowire under the electron beam irradiating. **b** Explains the growth process of metallic nanomushrooms on a nanowire. **c** The scanning transmission electron microscope (TEM) images show the growth process of the metallic nanomushrooms from the initial spore bud (indicated by the blue arrow point A) to the umbrella-like mature mushrooms stage. **d** The initial spore bud (left) and the umbrella-like mature mushrooms stage (right), the size of the spore is 8.21 nm, and the size of the mature mushrooms is 52.26 nm, respectively. **e** The initial spore bud and surrounding environment TEM image (indicated by the bule arrow point B). **f–h** TEM images and element mapping of metallic nanomushroom (aspect ratio $n = 3$ and 6, respectively) (scale bars: 100 nm).

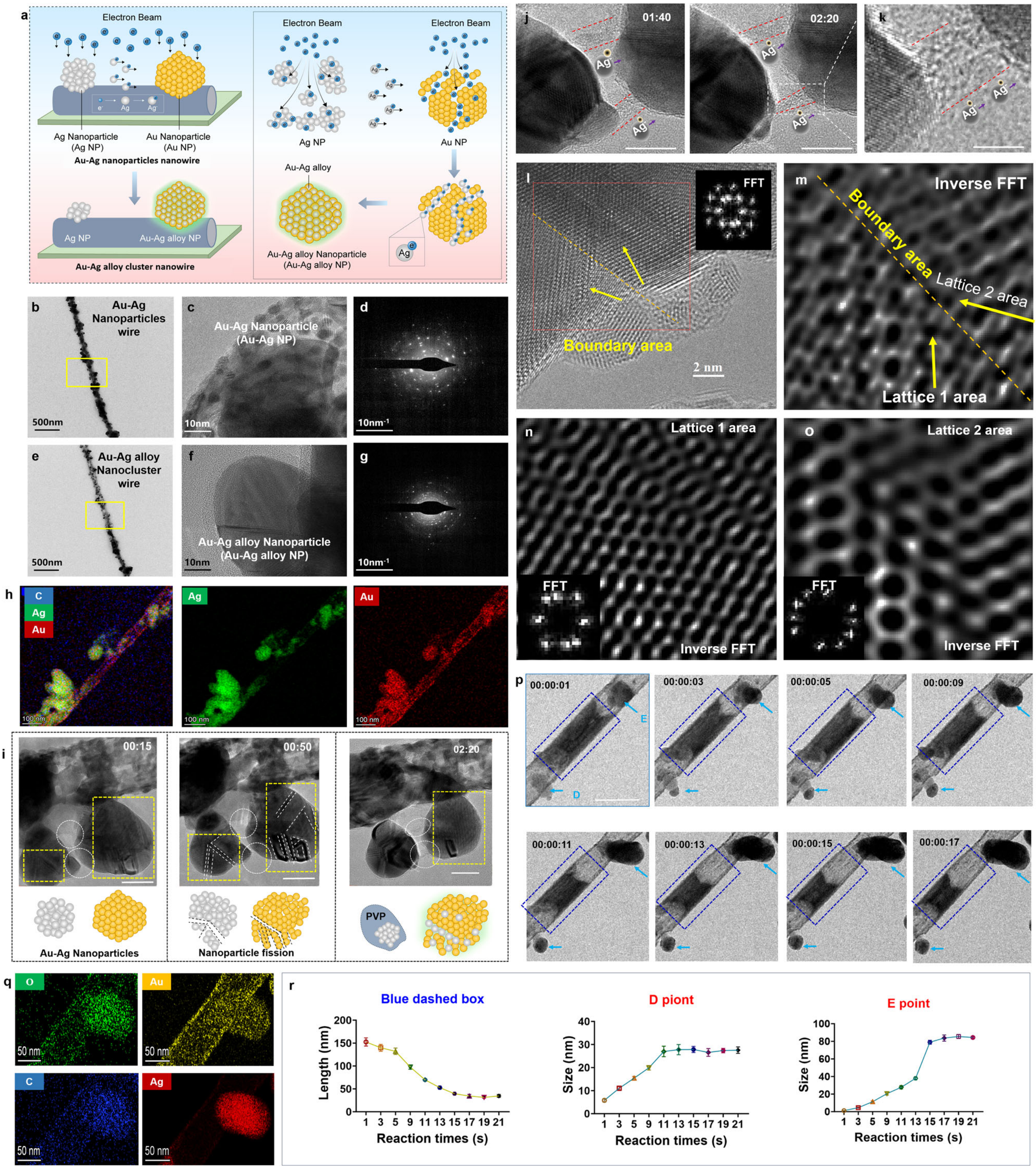

Fig. 2 | Analysis of growing targeted photoluminescent metallic nanomushrooms on nanowire. a The principle analysis diagram of the generation of metallic nanomushroom. The TEM image of Au–Ag nanoparticels wire (**b**), the Au–Ag nanoparticels TEM image (**c**), SAED image of Au–Ag nanoparticles (**d**). The TEM image of Au–Ag alloy nanomushroom wire (**e**), the Au–Ag alloy nanomushroom TEM image (**f**), SAED image of Au–Ag alloy nanomushroom (**g**). **h** TEM image and element mapping of the Au–Ag alloy nanomushroom. **i** The morphological state of Au and Ag nanoparticles over time under electron beam irradiation. The white dotted lines indicate the crack position of nanoparticles, and red arrows mark the position of atomic transfer in the nanoparticle. The magnified images of the regions marked with atomic transfer by the red dotted circles are shown in (**j**, **k**) when electron beam irradiation. The white dotted lines are Au nanoparticles; The red dotted lines are Ag nanoparticles. The structural changes inside the nanoparticles after the atoms are transferred to another nanoparticle are shown in the figures (**l**–**o**). **l** The lattice of the interface region where gold and silver atoms are squeezed was captured by TEM and SAED. Red dotted frame indicates TEM image and FFT of the lattice evolution area (**l**), inverse FFT image of the lattice evolution area (**m**), FFT and inverse FFT images of lattice 1 area (**n**) and lattice 2 area (**o**), respectively. **p**–**r** The concentration change of metal atoms on the nanowire of Au–Ag nanoparticles with the irradiation of the electron beam (**p**); the distribution of metal atoms within the blue dashed box nanowires; the red arrows mark the metallic nanomushrooms. **q** TEM images and element mapping of nanowire of metallic nanomushroom. **r** Statistically analyze the regional changes of metal atoms and the growth conditions of nano-mushrooms (at points D and E). All experiments were independently repeated three times for each Au–Ag nanomushroom sample, and data are presented as mean ± standard deviation (SD). For morphological characterization,10 distinct visual fields were randomly selected from each sample for statistical analysis of nanostructure dimensions.

Analysis of growing targeted photoluminescent metallic nanomushrooms on nanowire

In order to confirm that the formation of metallic nanomushrooms is related to electron beam irradiation and Ag atom activation, the details of the growth process were observed in real time using TEM. As shown in Fig. 2, based on the analysis, we have created an overview diagram of the formation process (Fig. 2a). It present that the Ag and Au nanoparticles on nanowire has been split by electron beam, and the Ag atoms, with a smaller atomic number than Au, are more susceptible to ionization by losing outer electrons, while Au atoms remain stable in their atomic state. Under electron beam irradiation, Au nanoparticles develop numerous fissures. Activated Ag ions are then attracted to these defects and migrate directionally to fill the gaps, causing the gold nanoparticles to expand at the apex as the silver content increases, as shown in Fig. 2a. Compared with STEM images of Au–Ag nanowires before and after electron beam irradiation (Fig. 2b–g), the post-irradiation nanowires exhibit significantly enhanced transparency, with a reduced number but increased volume of remaining nanoparticles on the nanowires (Fig. 2e). Concurrently, as shown in Fig. 2h, the element mapping of the Au–Ag alloy nanomushroom presents that Ag element (green) are abundantly observe on the nanomushrooms and almost disappear on the nanowire, while Au element (red) are evenly distributed on the nanowire that have nanomushrooms. Meanwhile, atomic composition analysis reveals a transition from the original ordered, single-phase nanostructure to disordered alloy structure, as evidenced by selected area electron diffraction (SAED) patterns, as shown in Fig. 2d, g. In the detailed images showing nanoparticles on nanowire at different time point during electron beam irradiation (Fig. 2i), cracks (dark streaks on the nanoparticles) appear in the nanoparticles at 15 s. By the 20 s, the cracks increase in number and size (marked with white dashed lines). By the 140 s, almost all of the cracks disappear, and the left nanoparticle vanishes (marked with a red dashed circle). Zooming in on the area circled by the red dashed line (Fig. 2j), flowing cloud-like features can be observed migrating from the left nanoparticle to the right (within the red dashed region). As the irradiation time increases, the area of these flowing features decreases, coinciding with the gradual disappearance of the left nanoparticle (Fig. 2k). (Detailed description in SM and Videos 1–6).

Moreover, the lattice of the interface region where gold and silver atoms are squeezed was captured by TEM and SAED. (as shown in Fig. 2l–o), the nanostructures of the two lattice states (two yellow arrows in red dotted frame) gradually approach each other, and lattice reconstruction occurs, forming distinct lattice structures (Fig. 2m). It reveals that the grown metallic nanomushrooms form an alloy structure through the mutual extrusion of Au and Ag (Fig. 2n, o). Therefore, from the TEM images showing the continuous changes of the nanowires as shown in Fig. 2p, r, with the increase of reaction time, the transparent length (blued dashed box in Fig. 2p) of the nanowire increases, while the nanostructures grown at both ends of the nanowire also keep increasing (The points D and E indicated by the red arrow in Fig. 2r). We can conclude that the nanostructures grown on the nanowire grow by absorbing metal atoms from the nanowire. In other words, the nanomushrooms on the nanowire grow by absorbing metal atoms from the nanowire, which is similar to the growth of natural mushrooms—where fungal spores absorb nutrients from wood to grow into umbrella-shaped mushrooms. As shown in Fig. 2q, the TEM images and element mapping of the nanowire of metallic nanomushroom further shown that there is almost no Ag (red) in the transparent segment of the nanowire, while a large number of silver atoms accumulate in the grown nanostructures. In contrast, Au (yellow) is uniformly distributed without aggregation at any specific location. Statistical measurements (Fig. 2r) demonstrate that subsequent to the 10th second, upon stabilization of the length of the transparent segment within the nanowire (as denoted by the blue dashed box in Fig. 2o), the nanostructures at both terminals (The points D and E indicated by the red arrow in Fig. 2o) cease to grow. This further corroborates that the growth of nanomushrooms is sustained by silver atoms originating from the nanowire.

The characterization of Au–Ag nanomushroom nanowire

Above, having established the growth mechanism of metallic nanomushrooms on nanowires, the optoelectronic properties of these alloy nanostructures (Au–Ag alloy nanomushroom nanowire, Au–Ag NMW) emerge as a critical focus in applied research. Accordingly, a comprehensive characterization of their properties was performed via atomic force microscopy (AFM), absorption/emission spectroscopy, and scanning transmission electron microscopy (TEM), as shown in Fig. 3. The TEM observations reveal that numerous metallic nanomushrooms emerge on the nanowire under electron beam irradiation (Fig. 3a–c). During this process, some spore-like sites (blued crow in Fig. 3a) are detected to disappear as they are absorbed by neighboring larger structures (red crow in Fig. 3a). Ultimately, the nanowire segments beneath the grown nanostructures become more transparent, and smaller nanostructures are also assimilated (Fig. 3c).

Meanwhile, conductivity measurements of nanowire densely populated with metallic nanomushrooms were performed using a high-resolution multi-mode atomic force microscope (the conductivity measurements were carried out using PeakForce TUNA contact mode, and the cantilever calibration was performed using the thermal noise method. The AFM-based conductivity measurements were performed using a bio-type high-speed atomic force microscope (FastScan Bio, Bruker)) as shown in Fig. 3d. Comparative analysis with pristine Ag nanowires reveals that the point potential of the nanowire densely populated with metallic nanomushrooms is nearly double that of their counterparts (Fig. 3e, f), while the peak current exhibits an enhancement of approach three orders of magnitude (Fig. 3g, h). Moreover, the results from statistical analysis of potentials and peak currents at different sites (points A, B, and C in Fig. 3e, g) comfier that nanowires with numerous metallic nanomushrooms exhibit greater advantages in conductivity. To verify the higher conductivity increase using an independent technique by conductive AFM with controlled tip pressure. As shown in Fig. 3i, the C–V curves at the positions of the Au–Ag nanomushroom and the Au–Ag nanowire were measured by controlling and varying the voltage (−0.2 to 0.2 V, step size: 0.05 V) applied to the AFM tip. The results indicate that the electrical conductivity of the nanomushroom is approach three orders of magnitude higher than that of the nanowire. It is means that such nanowires should also possess excellent performance in photothermal conversion, owing to the more unimpeded transport of electrons.

Among the characteristics above, the metallic nanomushrooms on nanowire consist of Au and Ag atoms, resulting in a structure analogous to molecular state, which constitutes a three-level system in terms of energy levels (Fig. 3k). Based on the transition process of excited-state electrons, the PL of metallic nanomushrooms is generally categorized into (1) fluorescence, originating from the S1 → S0 transition with the same spin multiplicity; (2) phosphorescence, involving an intersystem crossing process from S1 to T1 and the subsequent transition of T1 → S0 with changed spin multiplicity[22]. We characterized the emission spectra, fluorescence lifetimes, absorption spectra, and QYs of Au–Ag NWM and mushroom cap-free Au–Ag nanowires using a steady-state/transient fluorescence spectrometer. Analysis of the emission spectra revealed that Au–Ag NWM exhibits a distinct fluorescence peak at 550–600 nm, with a full width at half maximum of approximately 50 nm (Fig. 3l). Furthermore, the fluorescence intensity was found to be positively correlated with the nanomushroom density: the denser nanostructure (Au–Ag NWM2) displayed a higher fluorescence peak intensity than the less dense counterpart (Au–Ag NWM1). Notably, no fluorescence signal was detected for the mushroom cap-free Au–Ag nanowires. The fluorescence decay time of Au–Ag NWM was measured to characterize its excited-state dynamics. As shown in Fig. 3m, the decay curves of Au–Ag NWM and Au–Ag nanowires were well fitted with a bi-exponential decay model, yielding average decay times of $\tau_1 = 7.6$ ns (Au–Ag NWM) and $\tau_2 = 1.7$ ns (the mushroom cap-free Au–Ag nanowires), respectively. Complementary absorption spectra measurements further characterized the optical absorption properties of the two nanostructures. Across the excitation wavelength range of 250–550 nm, Au–Ag NWM exhibited a higher overall absorption efficiency than the mushroom cap-free Au–Ag nanowires (Fig. 3n). Specifically, in the ultraviolet region

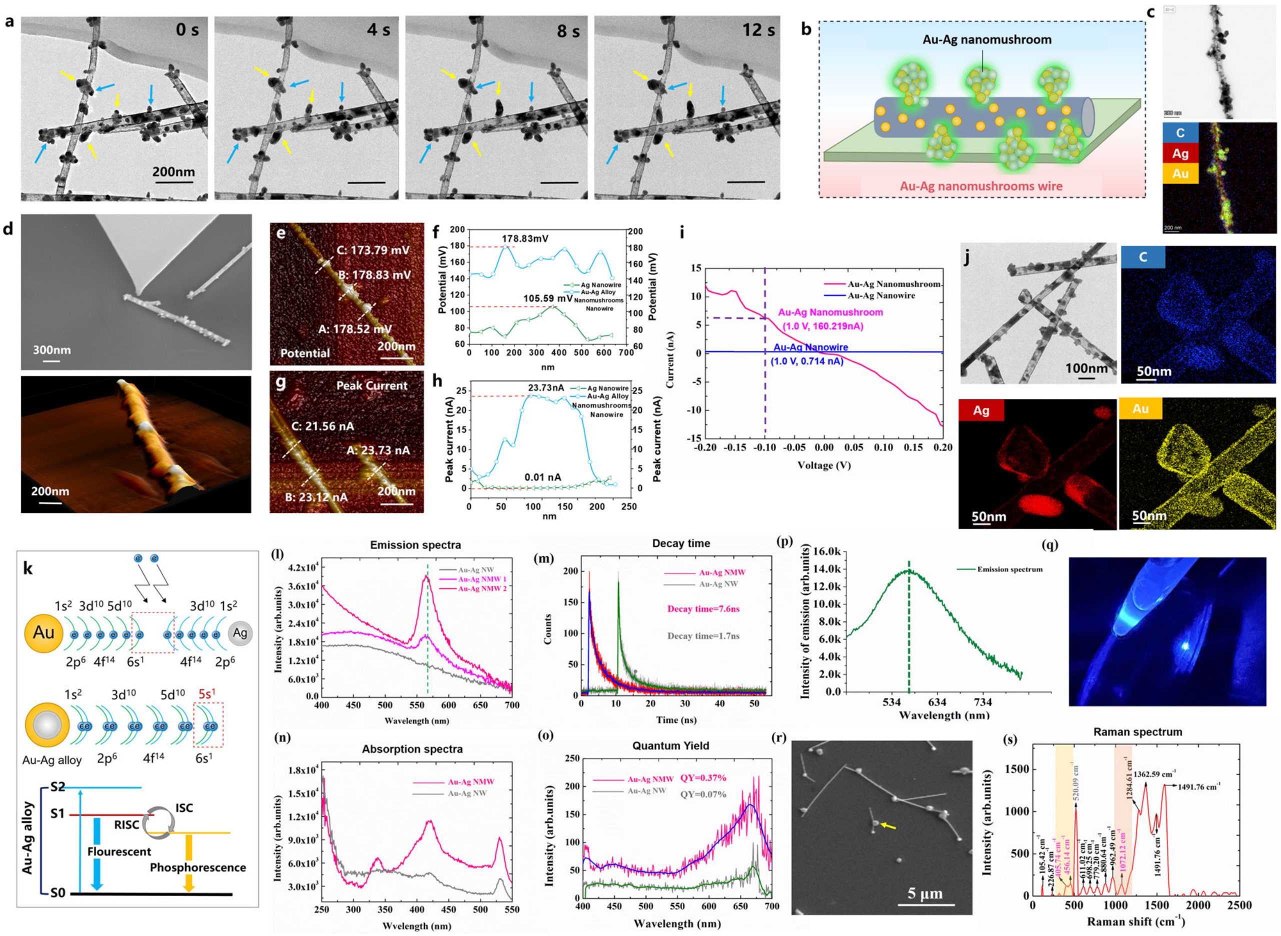

Fig. 3 | The characterization of Au–Ag nanomushroom nanowire. **a** TEM image of Au–Ag nanomushroom nanowire at different times when electron beam irradiation. The position of the red arrow is gradually growing; the position of the blue arrow is gradually shrinking. **b**, **c** TEM images and element mapping of metallic nanomushroom on the nanowire. **d** AFM image of Au–Ag nanomushroom on the nanowire. The potential of Au–Ag nanomushroom on the nanowire has been detected by AFM (**e**). Meanwhile, the peak current of Au–Ag nanomushroom on the nanowire has been detected by AFM (**g**). Therein, the A, B, and C are different positions Au–Ag nanomushroom on the nanowire. **f**, **h** The value of potential and peak current Au–Ag nanomushroom compared with Ag nanowire, and resulting statistics of potential and peak current in different positions. **i** The *C*–*V* curves at the positions of the Au–Ag nanomushroom and the Au–Ag nanowire were measured by controlling and varying the voltage 0.20–0.20 V. **j** TEM images and element mapping of nanowire of metallic nanomushroom. **k** The schematic diagram of electron arrangement in the alloy of Au and Ag, meanwhile the resulting energy band diagram. Emission spectra (**l**), decay time (**m**), absorption spectra (**n**) and quantum yield (**o**) of Au–Ag alloy nanomushroom nanowire and Au–Ag nanowire, respectively. **p** The fluorescence spectra and **q** photo emitted under the excitation of 405 nm lasing. Synchronous micro-Raman spectroscopy. **r** SEM image. **s** The Raman spectrum of nanomushroom (marked by a yellow arrow).

(<300 nm), the imaginary part of silver's dielectric constant assumes a positive value, which diminishes its metallic characteristics and consequently gives rise to a prominent absorption peak in this range.

We also determined the QYs of both nanostructures under 350 nm excitation. In Fig. 3o, experimental results demonstrated that Au–Ag NWM achieved a QY of 0.37%, whereas the mushroom cap-free Au–Ag nanowires exhibited a negligible QY of only 0.07%, which is close to zero. This finding is consistent with our emission spectroscopy data, as the mushroom cap-free Au–Ag nanowires showed almost no fluorescence emission. The results reveal that the absorption spectra remain invariant across different concentrations of nanomushrooms (Fig. 3l), with only the absorbance values increasing proportionally. Under 405-nm laser excitation, fluorescence emission was detected at a central wavelength of 560 nm (Fig. 3p, q). Analysis of the absorption and emission spectra confirms that these nanowires exhibit fluorescence capabilities, with the intensity increasing as the density of metallic nanomushrooms rises. Nevertheless, to clarify the Au/Ag atomic ratio during this process as well as the content of Au/Ag alloy within the nanomushrooms, we employed synchronous micro-Raman spectroscopy (WITec confocal Raman spectroscopy microscope RISE-MAGNA). Further scrutiny of the Raman spectra uncovered two closely overlapping peaks at 405.74 and 456.14 cm^{-1}, located to the left of the peak at 520.09 cm^{-1}. Based on reference data, these two peaks were identified as the characteristic peaks arising from the correlated compressive interactions between Au and Ag atoms within the lattice. Additionally, the peak at 1072.12 cm^{-1} was assigned to the characteristic Raman signal corresponding to the interactions between the formed Au/Ag alloy and polyvinylpyrrolidone (PVP).

Presentation of the process and characteristics of FA-Au–Ag NMW synthesis

To obtain the targeted tumor cells, the precise fabrication of FA-Au–Ag nanomushrooms nanowire (FA-Au–Ag NMW) is shown in Fig. 4a. The Au–Ag NMW were initially prepared and the detailed description of the processing on section II of the Supplementary materials. They were modified with SH-PEG2000-FA to synthesize FA-Au–Ag NMW. The sulfhydryl group reacted with Au in the FA-Au–Ag NMW through Au–S bonds. Scanning TEM images and elemental mapping revealed the formation of high density of FA molecules on Au nanoparticles the surface of FA-Au–Ag NMW (Fig. 4b). Therein, carbon (blue) and oxygen (green) elements cover the surface of the Au–Ag nanomushrooms on the nanowire. It is means that the FA molecules has been linked to Au–Ag nanomushrooms. This thus

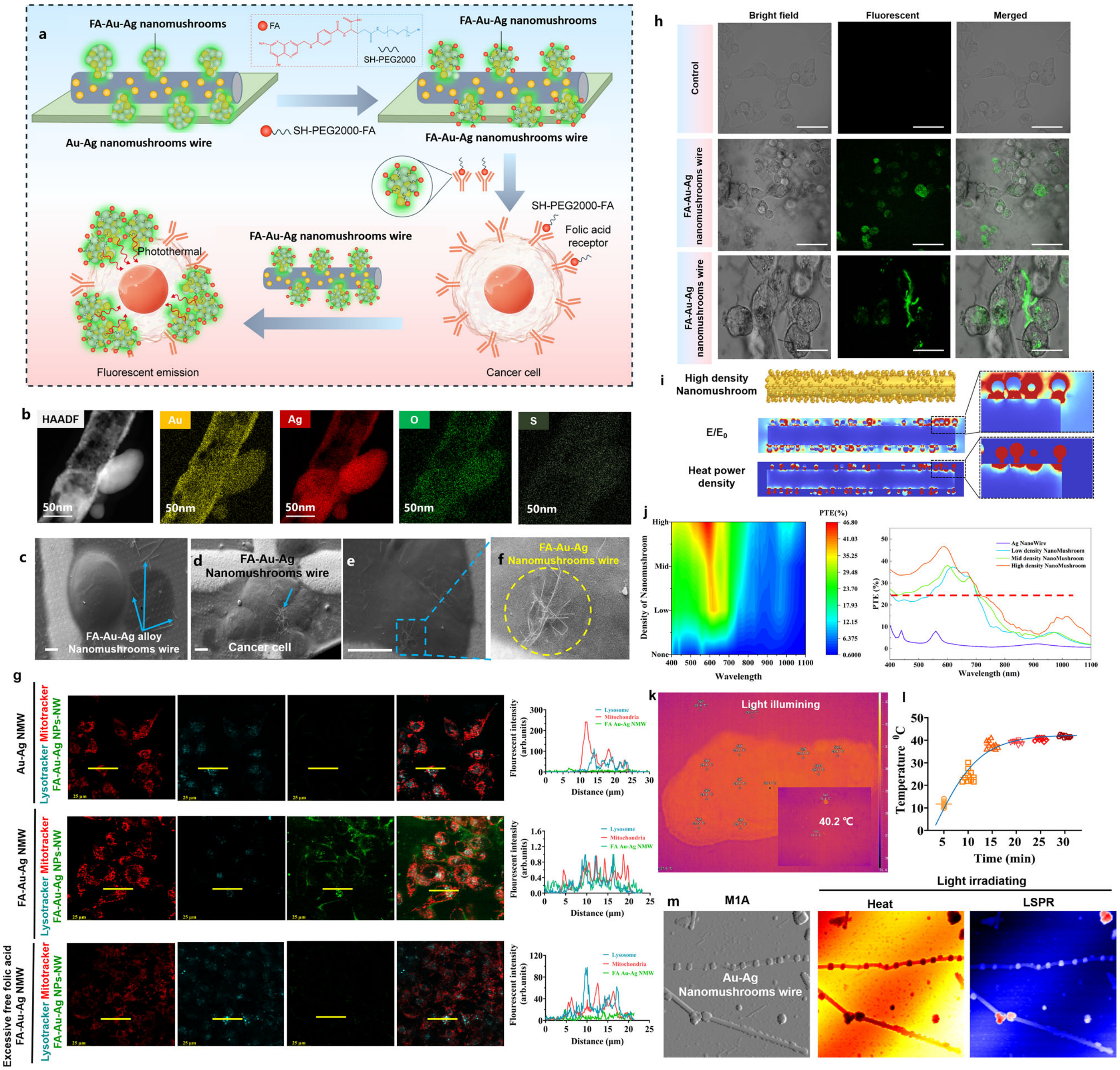

Fig. 4 | Presentation of the process and characteristics of FA-Au–Ag nanomushroom nanowire synthesis. a FA-Au–Ag nanomushroom wire synthesis process. **b** TEM images and element mapping of FA-Au–Ag nanomushroom nanowire. Yellow, red, green and blue are Au, Ag, O, and C, respectively. **c**, **d** The cryo-electron microscopy images of FA-Au–Ag nanomushroom wire were taken after culture with normal cells or cancer cells, respectively (the detailed description of cryo-electron microscopy images in section II of the Supplementary material). **e**, **f** the cancer cell and FA Au–Ag nanomushrooms nanowire. **g** For the folate receptor competition assay, A2780 cells were allocated into four groups as follows: Au–Ag NWs; FA-Au–Ag NMWs; and pre-incubation with excess free folate (30 min) prior to treatment with FA-Au–Ag NMWs. **h** The fluorescent images of nanomushroom wire by confocal laser scanning microscope. **i**, **j** COMSOL Multiphysics simulations show the electromagnetic field distribution and photothermal conversion efficiency (PTE) of pristine Ag nanowires and Au–Ag nanowires decorated with low-, medium-, and high-density nanomushrooms. The presence of Au–Ag nanomushrooms markedly enhances light absorption and photothermal conversion over a broad wavelength range, with increasing nanomushroom density leading to progressively higher PTE compared to bare Ag nanowires (**j**). **k** The macroscopic temperature rises of the entire solution volume containing Au–Ag NMWs under light irradiation, temperature elevation curves **l**, the temperature map generated under the 100 mW LED irradiation 10 min is tested by micro-heat distribution test system (the detailed description of test processing in section III of Supplementary material). **m** The surface plasma of Au–Ag NPs-NW with different Au particles density by the AFM-IR. The relative intensity of the SPR of gold nanoparticles on the surface of the scanning nanowire by neaSNOM, therein, the red represents the relative intensity of the SPR on the surface of a nanomushroom and the relative intensity distributions of surface plasmon. (scale bar: 50 nm).

indicates that nanowires bearing Au–Ag nanomushrooms, upon conjugation with folic acid molecules, gain the capacity to target tumor cells with overexpressed folate receptors.

To demonstrate that FA-Au–Ag NMW has the property of targeting tumor cells, the FA-Au–Ag NMW were taken culture with normal ovarian cells (SK-OV-3 (RRID: CVCL_0C84)) and the human ovarian cancer cell (A2780 (RRID: CVCL_0134)) 2 h, the position relationship between cells and FA-Au–Ag NMW was observed by Cryo-electron microscopy images of in vivo, respectively (The detailed description of processing on section IV of Supplementary materials). In Fig. 4c–f, the FA-Au–Ag NMW were scattered around the normal cells and the surface of cells is not attached nanowires (Fig. 4c). On the contrary, a large number of FA-Au–Ag NMW were accumulated and attached on the surface of ovarian cancer cells (Fig. 4d–f). According to these results of TEM and cryo-electron microscopy, it is significantly reveals that FA-Au–Ag NMW have the property of actively targeting tumor cells. Meanwhile, for the folate receptor competition assay to distinguish surface binding, A2780 cells were allocated into three groups as follows: (1) Au–Ag NMWs; (3) folate-conjugated Au–Ag NMW (FA-Au–Ag NMWs); and (3) pre-incubation with excess free folate (30 min) prior to treatment with FA-Au–Ag NMWs. As illustrated in Fig. 4g, comparative analysis revealed distinct differences between group 1, group 2, and group 3: in group 2, extensive nanowire accumulation (green fluorescence) was observed on and within cells post-treatment, whereas nanowire signals (green fluorescence) were markedly diminished in group 3. Compared with the second group of experiments, no green fluorescence of FA-Au–Ag NMW was observed around the cells in the first group. Therefore, it can be concluded that FA-Au–Ag NMW is linked to the tumor cells through folic acid and the folic acid receptors on the cells. Furthermore, this finding indicates that excess free folate competitively occupied folate receptors on the cell surface, preventing folate-conjugated nanowires from binding to the cell membrane. Consequently, cells were not subjected to heat-induced apoptotic damage mediated by nanowires.

Moreover, the presence of numerous PL Au–Ag NMW enabled visualization of tumor cells via emitted fluorescence in the laser beam by laser confocal microscopy, as shown in Fig. 4h. Under the ×100 magnification, one can observe that green fluorescence is emitted from the fibrous nanowires that are close to the cell membrane. As we know that the LSPR of metal nanoparticles is closely related to the free electrons and frequency of excited light[23]. Therefore, the Au–Ag alloy nanomushrooms provide nature condition to generate the LSPR used the light irradiation. In principle, the improvement of the photothermal conversion can be achieved by suppressing the light scattering and/or increasing the light absorption of plasmonic nanostructured particles (PNPs) at LSPR. Therein, the photothermal conversion effect of PNPs is inversely proportional to their conductivity[24]. As shown in Fig. 4i, j, we compared with heat power density, absorption cross section, and photothermal efficiency on the surface of Ag nanowire and Au–Ag NMW under the wide band light spectrum LED (400–1400 nm) by COMSOL numerical stimulation (section III of Supplementary material). The results show that heat power density, absorption cross section and photothermal efficiency of Au–Ag NMW (Fig. 4i, j) are much higher than Ag nanowire without Au nanoparticles under the light irradiation. Therein, the photothermal efficiency of Au–Ag NPs-NW absorption of LED light reaches more than 32% on average (400–1100 nm), which is much higher than that of nanowire efficiency of about less than 2% (Fig. 4j). Regarding Fig. 4k, l, we would like to clarify that the reported temperature increase to 40.2 °C represents the macroscopic temperature rise of the entire solution volume containing Au–Ag NMW under light irradiation. This measurement was intentionally included to demonstrate the overall bulk heating behavior under biologically relevant and mild irradiation conditions. Due to heat dissipation into the surrounding medium and the relatively large solution volume, the macroscopic temperature increase is inherently limited and does not directly reflect the local photothermal intensity at the nanoparticle-cell interface. Therefore, to verify the LSPR of the fabricated Au–Ag NMW, the AFM-IR (neaSNOM, Germany, its performance: mid-infrared QCL laser, operating range 920–1815 cm^{-1}, compatible with continuous wavelength mode, spectral resolution: 1 cm^{-1}; Visible light laser 633 nm; The spatial resolution of nano-infrared is ≤10 nm. Scanning range: 100 μm × 100 μm × 2.8 μm) was employed to map the spatial distribution of surface plasmon polaritons in Au NPs of Au–Ag NMW with a spatial resolution of ~10 nm. As depicted in Fig. 4m, the AFM-IR was used to characterize the LSPR enhancement and nanoscale energy confinement of the Au–Ag NMW hybrid platform under white light excitation. The AFM-IR amplitude images (Fig. 4m) show that the near-field electric field intensity at the Au–Ag nanomushroom deposition sites is enhanced to the bare Ag NWs, with the enhancement factor increasing with Au NPs density. The phase images further confirm that the localized plasmonic field is confined within a spatial range of ~10 nm from the nanomaterial surface, consistent with the formation of high-density LSPR. These AFM-IR results, together with theory and simulation, directly verified the nanoscale plasmonic mechanism of the hybrid platform, supporting its superior photothermal conversion efficiency and tumor therapy potential. Consequently, the abundant growth of metallic nanomushrooms on the nanowire directly elevates fluorescence intensity, meanwhile, the LSPR induced by these nanomushrooms enables resonant amplification of fluorescence and conductivity.

In vitro experiments and analysis

In order to verify the inhibitory effect of as-synthesized FA-Au–Ag NMW as photothermal agents against tumor cells under the light irradiation, we compared with flow cytometry and laser confocal microscopy results of the normal cells and the ovarian cancer cells has taken culture through FA-Au–Ag NMW and light irradiation (the power density of LED is 0.21 mW/mm^2 = 210 mW/cm^2 (In fact, our actual effective area is on the order of millimeters.), respectively. As shown in Fig. 5, from the fluorescence images of ovarian cancer cells, it could be observed that the FA-Au–Ag NMW combined with light irradiation caused large amounts of red fluorescence within the cells, and the green fluorescence was noticeably reduced, which was a sign of cell death (Fig. 5a, b).

In contrast, in the other groups with low concentration of FA-Au–Ag NMW or without light irradiation, extensive live cells were detected, as well as no obvious death (Fig. 5c–e). These results from the live/dead observation were in accordance with those from the flow cytometry experiment, where both types of results showed that FA-Au–Ag NMW could selectively kill cancer cells while having negligible effect on normal cells when triggered by light, which is conducive for subsequent in vivo tests. As shown the above results, the photothermal conversion temperature of FA-Au–Ag NMW under the light irradiation was 40.2 °C (Fig. 4k), which was not ability to induce cells apoptosis compared with the mild-temperature PTT 45 °C[25]. It was also confirmed from the expression of heat shock response 70 (HSP70a1β) and HSP90aa1 by qPCR, in Fig. 5f, g. That's because cellular HSP causes a rapid overexpression of HSPs, such as HSP70a1β and HSP90aa1, during PTT treatment to thermoresistance of the cancer cells against heat stress.

In conventional photothermal therapy (PTT), the upregulated expression of heat shock proteins (HSPs) is a well-documented indicator of augmented cellular tolerance to thermal damage and enhanced self-repair potential, with HSP expression levels exhibiting a direct positive correlation with the magnitude of thermal injury sustained by cells. Accordingly, suppressing HSP expression has long been regarded as a viable strategy to improve the antitumor efficacy of traditional PTT. Indeed, the HSP-mediated repair of heat-induced cellular damage is a time-dependent process that requires sufficient time for accumulation. Only when thermal damage is induced at a slow rate can tumor cells initiate effective repair mechanisms to counteract heat-triggered apoptosis. In stark contrast, we hypothesize that ultrafast thermal damage induction can decouple the cytoprotective function of HSPs from their stress-induced upregulation: although high HSP expression still serves as a biomarker of severe thermal injury, the extremely rapid onset of damage deprives cells of the time required to execute HSP-mediated repair programs, thereby shifting the cellular response toward apoptosis. Thus, A2780 cells were treated with HSP agonist (tamoxifen) or HSP inhibitor (17-AAG), and subsequent phenotypic alterations were monitored to dissect the mechanistic role of HSPs in modulating the therapeutic outcome of our ultrafast PTT approach. Using confocal laser scanning microscopy, we imaged the intracellular morphology of cells under three treatment conditions—pure FA-Au–Ag NMW, HSP agonist, and HSP inhibitor alone—following 20 min of LED irradiation. The results showed that the FA-Au–Ag NMW (green) would target the tumor cells, and at the same time, severe damage occurred to the cell membrane, leading to cell apoptosis and lysis.

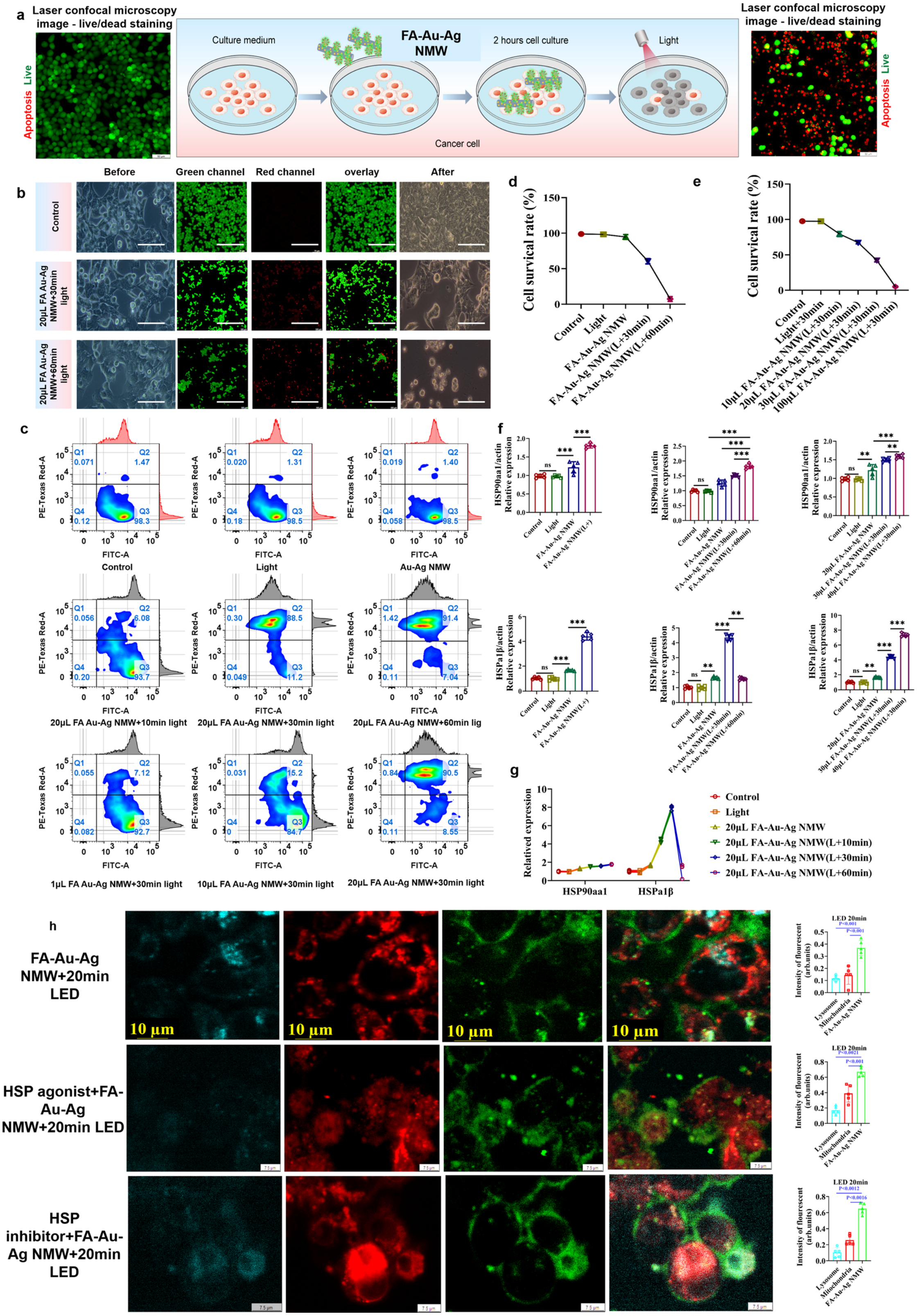

Fig. 5 | Testing the ability of FA-Au–Ag NMW to kill tumor cells under the LED irradiation. a The experimental flowchart for killing cancer cells. **b** Live/dead staining images of ovarian cancer cells with various treatments (scale bar: 250 μm). Cell viability of (**b**) ovarian cancer cells after incubation 48 h with the same concentrations of FA Au–Ag nanomushroom wire in the presence under the 30 and 60 min light irradiation or the absence of light and FA-Au–Ag nanomushroom wire. **c** Analyze the viability rate of cancer cells under the different experimental conditions by Flow cytometry. **d**, **e** The cell survival rate of cells under the different conditions, such as kinds of FA-Au–Ag nanomushroom wire concentrations and light irradiations. **f**, **g** The relative protein expression levels of HSP90 and HSP70 under the FA-Au–Ag nanomushrooms wire and Light irradiation. ns. $*p < 0.1$, $**p < 0.01$ and $***p < 0.001$ analyzed by Student's *t* test. **h** Laser confocal microscope fluorescence image: pure FA-Au–Ag NMW, HSP agonist, and HSP inhibitor alone—following 20 min of LED irradiation. The *p*-value has been provided.

Thus, we studied cell morphology and cell gene expression by flow cytometry and laser confocal microscopy techniques to find out the causes of apoptosis under FA-Au–Ag NMW combined with light irradiation.

Conclusions

In summary, we have developed FA-Au–Ag NMW with robust targeting capabilities and strong PL through a straightforward and high effective physical approach. This nanostructure inherently exhibits molecular-like fluorescence emission, while its alloy composition with high conductivity significantly enhances photothermal conversion efficiency. The mushroom-shaped nanostructure further provides a platform for high-density targeting molecule loading. Leveraging this nanomaterial, we can achieve exceptional targeting functionality, visualize targeted cells via enhanced fluorescence emission, and utilize photothermal effects to destroy and eliminate tissues, such as receptor-overexpressing cells. Based on experimental testing and result analysis, this nanostructure offers a dual-modal approach for both tracing and therapy in biomedicine, addressing the current bottlenecks in the application of photoluminescent nanostructures.

Materials and methods

Materials

The human ovarian cancer cell lines SK-OV-3 (RRID: CVCL_0C84) and A2780 (RRID: CVCL_0134) were purchased from Shanghai Zhongqiao Xinzhou Biotechnology Co., Ltd. (Shanghai, China). Cells were maintained in RPMI 1640 medium (ATCC modification, Gibco, Thermo Fisher, USA) supplemented with 10% fetal bovine serum (FBS) (Hyclone, Thermo Fisher, USA), 2 mM glutamine (Corning, USA) and 1% penicillin/streptomycin (Corning, USA) at 37 °C under 5% CO_2 in a humidified incubator. Culture medium: DMEM high glucose w/L-glutamine w/sodium pyruvate, 500 mL/bottle. PBS: phosphate-buffered saline w/o calcium w/o magnesium, 500 mL/bottle. FBS: Australia, USDA-approved/extra FBS, 500 mL/bottle. Antibiotic: antibiotic-antimycotic 100×, 100 mL/bottle. Complete culture medium was prepared by supplementing DMEM with 10% FBS and 1% antibiotics (v/v). Cell viability was evaluated using the Live/Dead Viability/Cytotoxicity Assay Kit (KGI; Calcein AM/PI method, 1000 tests), with excitation/emission wavelengths of 495/520 nm for Calcein AM and 530/620 nm for PI. Gold Mesh (Quantifoil, R 1.2/1.3, 300 mesh Au) was employed for electron microscopy.

Cell cultures were maintained in a CO_2incubator (HCP-168E, Haier Biomedical, Qingdao, China). LED light: bull, 30 W; yee LED light, 10.8 W. Cryo-electron microscopy was performed at an operating temperature of −165 °C using a Zeiss instrument. Ultra-high resolution multi-photon laser confocal microscope for live cells TCS SP8 STED 3X) located in Laboratory W251, Translational Medicine Building, Minhang Campus, Shanghai Jiao Tong University. High-resolution laser confocal microscope (Leica STELLARIS 5) in Laboratory W250, Translational Medicine Building, Minhang Campus, Shanghai Jiao Tong University. Both systems followed comparable operating procedures and yielded consistent imaging results.

Methods

Photochemical tumor treatment of ovarian cancer tumor cells (a2780). 1. Silver folic acid-functionalized nanowires decorated with gold nanomushrooms (FA-Au–Ag NMWs) were prepared. 2. The diluted FA-Au–Ag NMWs solution was added to petri dishes containing adherent A2780 cells in complete culture medium to reach a final concentration of 2% (20 μL/mL) or 5%, depending on the experimental gradient. Typically, 10 mL of medium was used per 10 cm dish, and 2 mL per well in six-well plates. 3. The culture dishes were then incubated under standard conditions for 2 h to allow sufficient interaction and binding between the Au–Ag NMWs and the cells. 4. After incubation, the dishes were removed and examined using an inverted microscope, revealing substantial nanowire deposition at the bottom of the culture dishes. 5. The culture medium was aspirated, and the cells were gently washed with PBS. This washing step was repeated twice, after which fresh complete culture medium was added. 6. Finally, the cell culture dishes were exposed to LED light irradiation, with the exposure duration adjusted according to the experimental gradient design.

Live and dead staining by confocal microscopy. 1. Prior to use, the stock solutions of Calcein AM and PI were equilibrated at room temperature for 30 min. 2. To prepare an 8 μM PI working solution, 5 μL of 16 mM PI stock solution was added to 10 mL of PBS and mixed thoroughly by vortexing. 3. Subsequently, 5 μL of 4 mM Calcein AM stock solution was introduced into 10 mL of the prepared PI solution, followed by vigorous mixing to ensure homogeneity. 4. As Calcein AM is susceptible to hydrolysis in aqueous solutions, the staining solution was freshly prepared and used on the same day. 5. Before staining, adherent cells were gently washed with PBS to remove residual culture medium. 6. An adequate amount of the working solution was added to the cells, ensuring complete coverage of the cell monolayer. 7. The cells were incubated at room temperature for 30–45 min. 8. After incubation, the staining solution was removed, the cells were washed with PBS, and the samples were prepared for confocal microscopy imaging. 9. Turn on the confocal microscope in advance. Select the appropriate excitation and emission bands based on the Ex/Em wavelengths of the live and dead dyes. 10. Confocal images were recorded and saved for subsequent analysis.

Flow fluorescence staining. 1. Collect and then centrifuge the cells, followed by two washes with PBS to remove residual culture medium. 2. Prepare the live-dead reagent working solution according to the confocal live-dead staining protocol. 3. Dilute the live-dead reagent with PBS at a ratio of 1:1000, and 200 μL of this working solution was added to the cell pellet. Cells were gently resuspended by pipetting and incubated at room temperature for 15–30 min for staining. 4. Select the suitable channel for the live-dead reagent. 5. Double-negative and single-stained controls were prepared to define the quadrant gates, and voltage and compensation settings were adjusted to achieve optimal signal detection. 6. The established cross-gate settings were applied to all samples to ensure consistent analysis. 7. Following these adjustments, perform on-line testing, ensuring the flow rate is set so that the number of events is controlled at 1000 cells/s. 8. Observe the proportions of living and dead cells, according to their distribution within the quadrant gate.

The cell counting kit-8 (CCK8). The cell counting kit-8 assay was performed to evaluate the cytotoxicity of FA-Au–Ag NMWs without light irradiation, as well as the proliferative activity of A2780 cells under different treatment conditions. Briefly, A2780 cells were seeded into 96-well plates at a density of 5×10^3 cells per well and incubated at 37 °C with 5% CO_2 for 24 h to allow cell adhesion. Afterward, cells were treated with various formulations (e.g., 2, 5, 10, 20, and 40% FA-Au–Ag NMWs solutions) and cultured for an additional 24 h. At the end of incubation, 10 μL of CCK8 reagent was added to each well, followed by incubation at 37 °C for 2 h. The absorbance at 450 nm was measured using a microplate reader (Bio-Rad, USA). Cell viability was calculated as the percentage relative to the control group (untreated cells), using the formula: cell viability (%) = (OD_{450} of treated group/OD_{450} of control group) × 100. All experiments were performed in triplicate, and data were expressed as mean ± standard deviation (SD).

Cryo-electron microscopy experiment. 1. Place the sterile gold mesh required for cryo-electron microscopy at the bottom of the culture dish before seeding the cells. After which, seed the cells onto the plate, so that the cells grow on the gold mesh. 2. The photochemical treatment of A2780 cells and corresponding controls was conducted according to the previously described cell culture protocol. 3. To preserve their structure, perform high-pressure freezing of the cells. 4. Cryo-scattering electron imaging (CSEI) was employed for the localization and analysis of cellular ultrastructure. 5. Capture the CryoEM images, and cryo-electron tomography (CryoET) data were collected to achieve high-resolution visualization. 6. Process the collected images. 7. Motion analysis was performed, with detailed procedures provided in the Supplementary materials.

AFM-based conductivity experiments. The current–voltage ($C–V$) characteristics at the positions of Au–Ag nanomushrooms and Au–Ag nanowires were measured by controlling and sweeping the bias voltage applied to the AFM probe from −0.20 V to 0.20 V with a step size of 0.05 V. Conductivity measurements were performed using PeakForce TUNA contact mode, and the cantilever was calibrated via the thermal noise method. All AFM-based conductivity experiments were carried out on a bio-type high-speed atomic force microscope (FastScan Bio, Bruker) at the Analytical and Testing Center of Shanghai Jiao Tong University (Room W230–W230).

Data availability

The data that support the findings of this study are available within the article and its Supplementary Information files.

Received: 13 September 2025; Accepted: 24 February 2026;
Published online: 23 March 2026

References

1. Fichthorn, K. A. Theory of anisotropic metal nanostructures. *Chem. Rev.* **123**, 4146–4183 (2023).
2. Kossak, A. E. et al. Anisotropic and multicomponent nanostructures by controlled symmetry breaking of metal halide intermediates. *Nano Lett.* **18**, 2324–2328 (2018).
3. Tang, Z. & Wei, A. Fabrication of anisotropic metal nanostructures using innovations in template-assisted lithography. *ACS Nano* **6**, 998–1003 (2012).
4. Gilroy, K. D. et al. Transformation of truncated gold octahedrons into triangular nanoprisms through the heterogeneous nucleation of silver. *Nanoscale* **7**, 6827–6835 (2015).
5. Huergo, M. A. et al. Optical nanoparticle sorting elucidates synthesis of plasmonic nanotriangles. *ACS Nano* **10**, 3614–3621 (2016).
6. Maturi, M. et al. Synthesis of ultrasmall single-crystal gold-silver alloy nanotriangles and their application in photothermal therapy. *Nanomaterials* **11**, 11 (2021).
7. Haddadnezhad, M. et al. Plasmonic double-walled nanoframes with face-to-face nanogaps for strong SERS activity. *Nano Lett.* **23**, 6831–6838 (2023).
8. Kadkhoda, J., Tarighatnia, A., Barar, J., Aghanejad, A. & Davaran, S. Recent advances and trends in nanoparticles based photothermal and photodynamic therapy. *Photodiagnosis Photodyn. Ther.* **37**, 102697 (2022).
9. Wang, W. X. et al. Seed-mediated growth of Au nanorings with size control on Pd ultrathin nanosheets and their tunable surface plasmonic properties. *Nanoscale* **8**, 3704–3710 (2016).
10. Zorlu, T., Correa-Duarte, M. A. & Alvarez-Puebla, R. A. Composite nanoparticle-metal-organic frameworks for SERS sensing. *J. Chem. Phys.* **158**, 18 (2023).
11. Jin, R. C., Zeng, C. J., Zhou, M. & Chen, Y. X. Atomically precise colloidal metal nanoclusters and nanoparticles: fundamentals and opportunities. *Chem. Rev.* **116**, 10346–10413 (2016).
12. Chakraborty, I. & Pradeep, T. Atomically precise clusters of noble metals: emerging link between atoms and nanoparticles. *Chem. Rev.* **117**, 8208–8271 (2017).
13. Kang, X., Li, Y. W., Zhu, M. Z. & Jin, R. C. Atomically precise alloy nanoclusters: syntheses, structures, and properties. *Chem. Soc. Rev.* **49**, 6443–6514 (2020).
14. Tang, Q., Hu, G. X., Fung, V. & Jiang, D. E. Insights into interfaces, stability, electronic properties, and catalytic activities of atomically precise metal nanoclusters from first principles. *Acc. Chem. Res.* **51**, 2793–2802 (2018).
15. Aikens, C. M. Electronic and geometric structure, optical properties, and excited state behavior in atomically precise thiolate-stabilized noble metal nanoclusters. *Acc. Chem. Res.* **51**, 3065–3073 (2018).
16. AbdulHalim, L. G. et al. $Ag_{29}(BDT)_{12}(TPP)_4$: a tetravalent nanocluster. *J. Am. Chem. Soc.* **137**, 11970–11975 (2015).
17. Liu, H. L. et al. Atomic-precision gold clusters for NIR-II imaging. *Adv. Mater.* **31**, 9 (2019).
18. Jiang, X. Y., Du, B. J. & Zheng, J. Glutathione-mediated biotransformation in the liver modulates nanoparticle transport. *Nat. Nanotechnol.* **14**, 874 (2019).
19. Huang, R.-W. et al. Hypersensitive dual-function luminescence switching of a silver-chalcogenolate cluster-based metal–organic framework. *Nat. Chem.* **9**, 689–697 (2017).
20. Niesen, B. & Rand, B. P. Thin film metal nanocluster light-emitting devices. *Adv. Mater.* **26**, 1446–1449 (2014).
21. Galchenko, M., Black, A., Heymann, L. & Klinke, C. Field effect and photoconduction in Au_{25} nanoclusters films. *Adv. Mater.* **31**, 6 (2019).
22. Liu, Z., Luo, L. & Jin, R. Visible to NIR-II photoluminescence of atomically precise gold nanoclusters. *Adv. Mater.* **36**, 2309073 (2024).
23. Lu, W. et al. Photoacoustic imaging of living mouse brain vasculature using hollow gold nanospheres. *Biomaterials* **31**, 2617–2626 (2010).
24. Davis, M. E., Chen, Z. & Shin, D. M. Nanoparticle therapeutics: an emerging treatment modality for cancer. *Nat. Rev. Drug Discov.* **7**, 771–782 (2008).
25. Whitesell, L. & Lindquist, S. L. HSP90 and the chaperoning of cancer. *Nat. Rev. Cancer* **5**, 761–772 (2005).

Acknowledgements

Fundings for this work are the National Natural Science Foundation of China (NSFC) (12574361); the Shanghai Municipal Science and Technology Major Project (grant no.2019SHZDZX01-06); and the Natural Science Foundation of Shanghai (23ZR1428400).

Author contributions

H.D., X.C. designed the study. Y.Q., H.Q. carried out the experiments and analyzed the data. H.D., Y.Q. wrote the manuscript and processed some figures.

Competing interests

The authors declare no competing interests.

Additional information

Supplementary information The online version contains Supplementary material available at https://doi.org/10.1038/s43246-026-01125-w.

Correspondence and requests for materials should be addressed to Hailang Dai or Xianfeng Chen.

Peer review information *Communications Materials* thanks the anonymous reviewers for their contribution to the peer review of this work. A peer review file is available.